

Graphene Carbon Nanotube Carpets

Grown Using Binary Catalysts for

High-Performance Lithium Ion Capacitors—

Supporting Information

Rodrigo Villegas Salvatierra,^{†,#} Dante Zakhidov,^{†,#} Junwei Sha,^{†,‡,±,#} Nam Dong Kim,[†] Seoung-Ki

Lee,^{†,1} Abdul-Rahman O. Raji,[†] Naiqin Zhao,^{‡,±} and James M. Tour^{†,‡,§,}*

[†]Department of Chemistry, [‡]The NanoCarbon Center, and [§]Department of Materials Science and NanoEngineering,

Rice University, 6100 Main Street, Houston, Texas 77005, USA.

¹School of Materials Science and Engineering, Tianjin Key Laboratory of Composite and Functional Materials, Tianjin University, Tianjin 300350, China.

[±]Collaborative Innovation Center of Chemical Science and Engineering, Tianjin 300350, China.

**Email: tour@rice.edu*

[#]Authors have contributed equally

¹ Current address: Institute of Advanced Composite Materials, Korea Institute of Science and Technology, Joellabuk-do 565-905, Republic of Korea

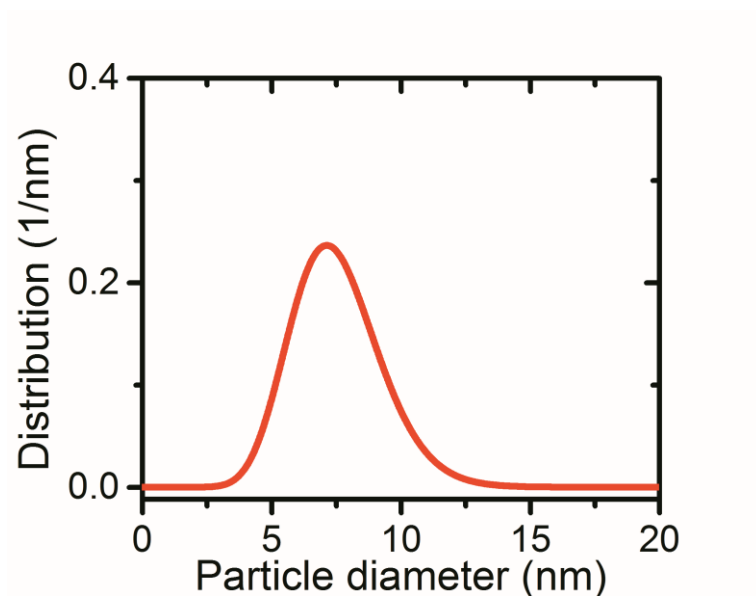


Figure S1. SAXS curve of Fe₃O₄ NPs in hexane produced by colloidal synthetic methods.

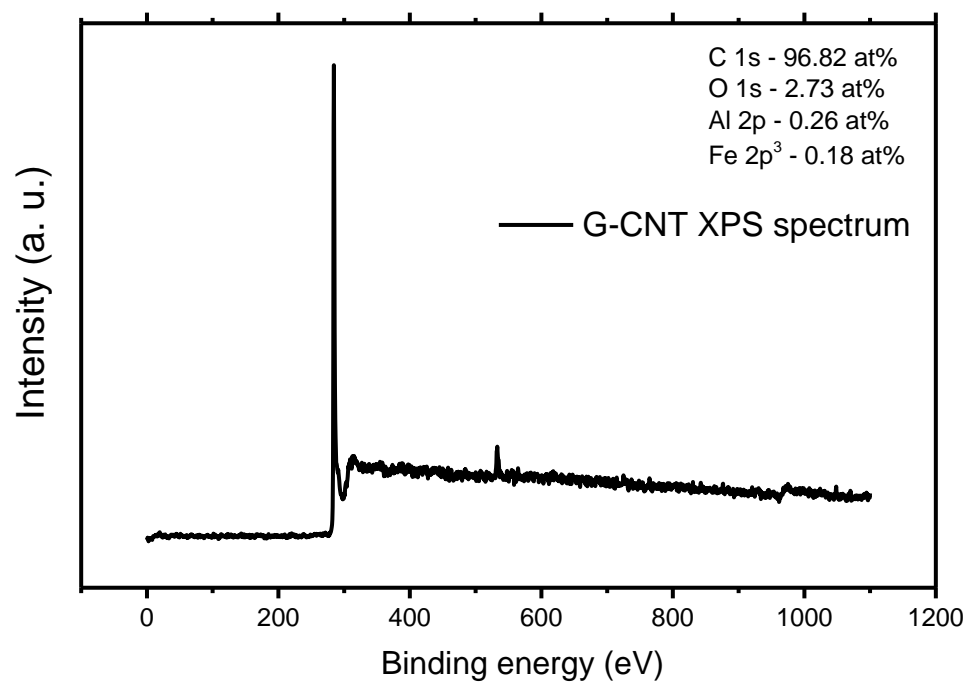


Figure S2. XPS long range spectrum of pure GCNT. Inset shows the calculated atomic proportion (at%) of C, O, Al and Fe.

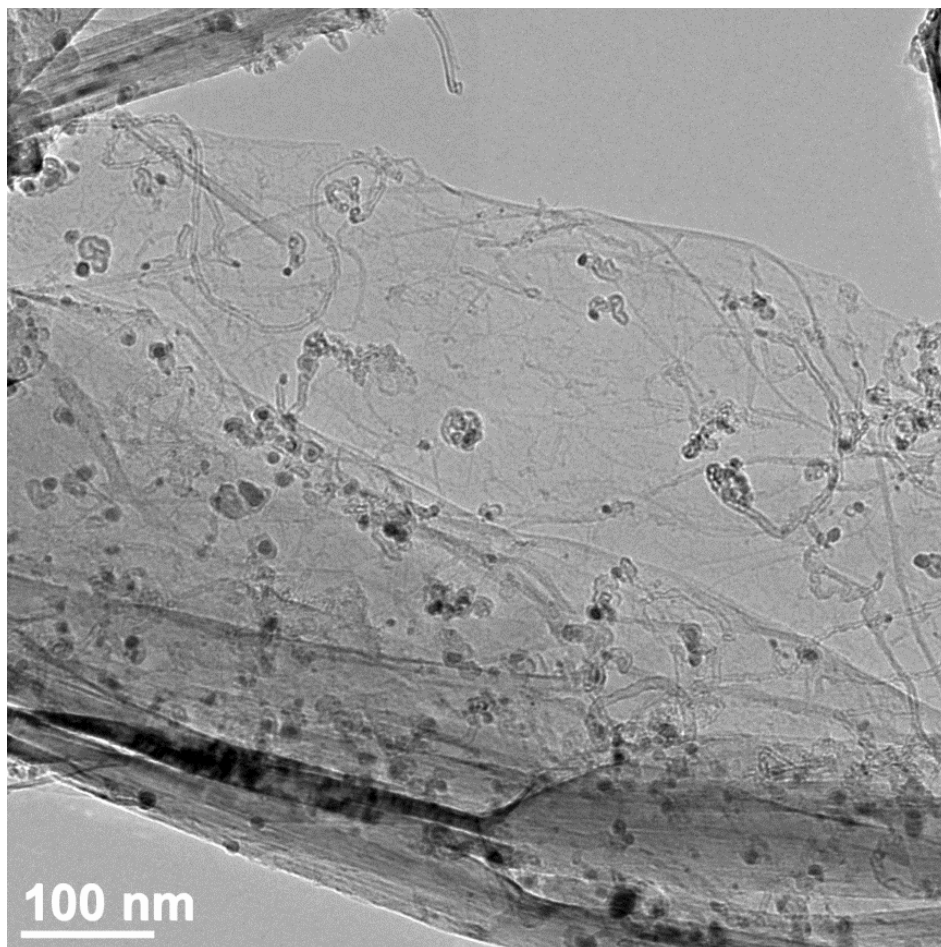


Figure S3. TEM image of GCNT produced over GNR substrate (low magnification).

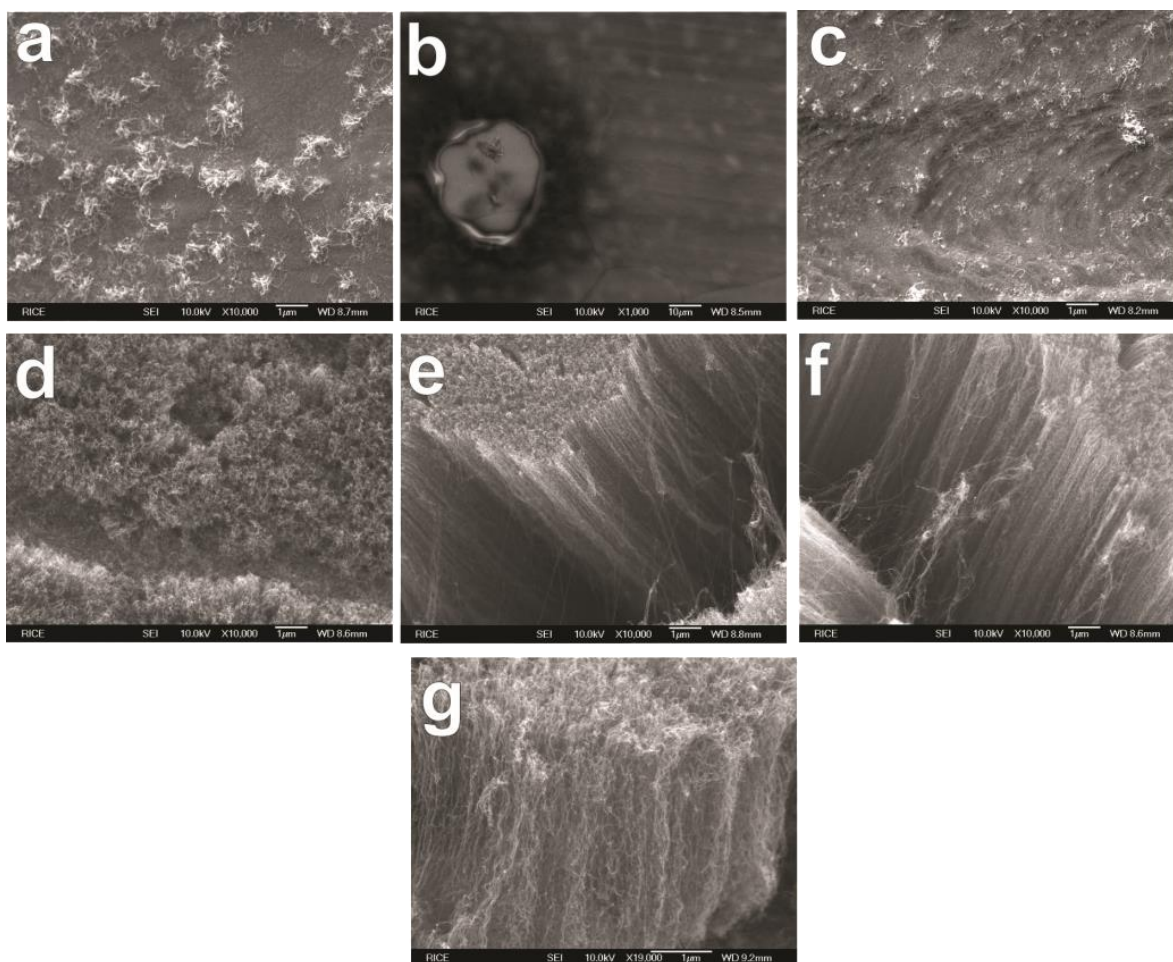


Figure S4. SEM images of carpets of GCNT produced with different catalysts solution. (a-b) GCNT produced from catalysts with only Fe_3O_4 or only AlO_x NPs (0 and 100 mol% Al content), respectively. (c-g) GCNT produced from binary catalysts with Al:Fe ratio 0.05:1, 0.2:1, 0.5:1, 1:1 and 2:1, respectively.

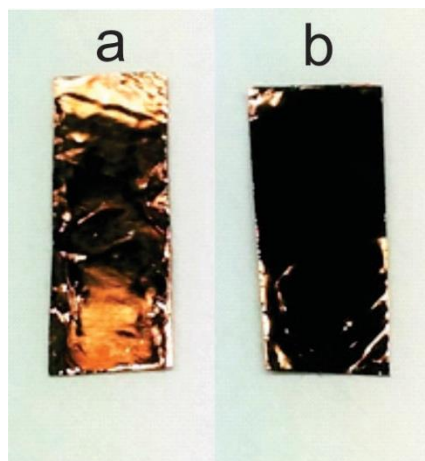


Figure S5. Photographs comparing deposition of catalysts. (a) GCNT produced from catalyst composed by spin-coating Fe_3O_4 NPs followed by AlO_x solution, (b) GCNT produced using $\text{Fe}_3\text{O}_4/\text{AlO}_x$ binary catalyst with 1:1 Al:Fe molar ratio.

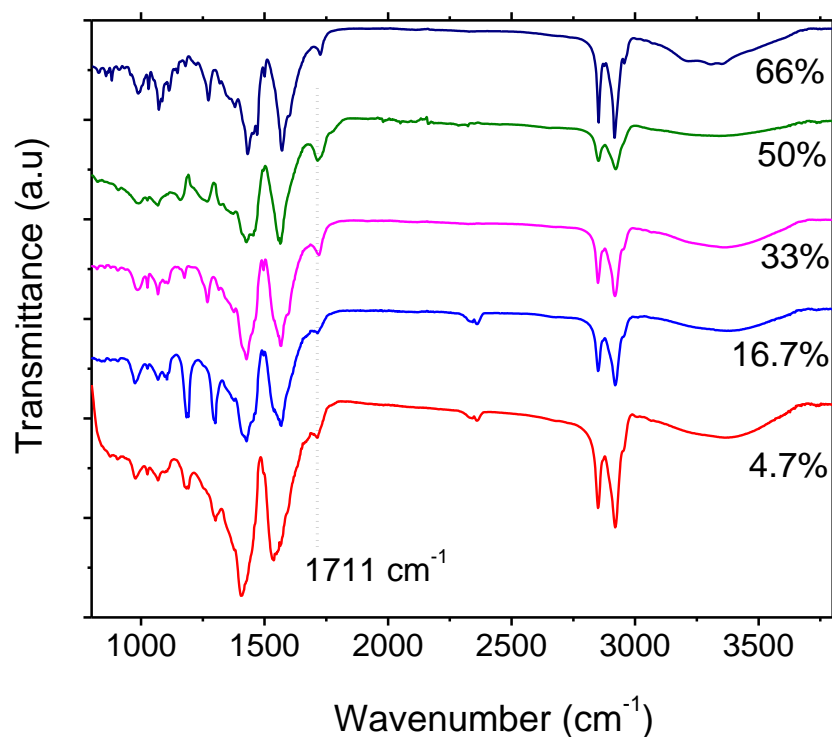


Figure S6. IR spectra of binary catalysts $\text{Fe}_3\text{O}_4/\text{AlO}_x$ with different Al content (4.7 to 66 mol%).

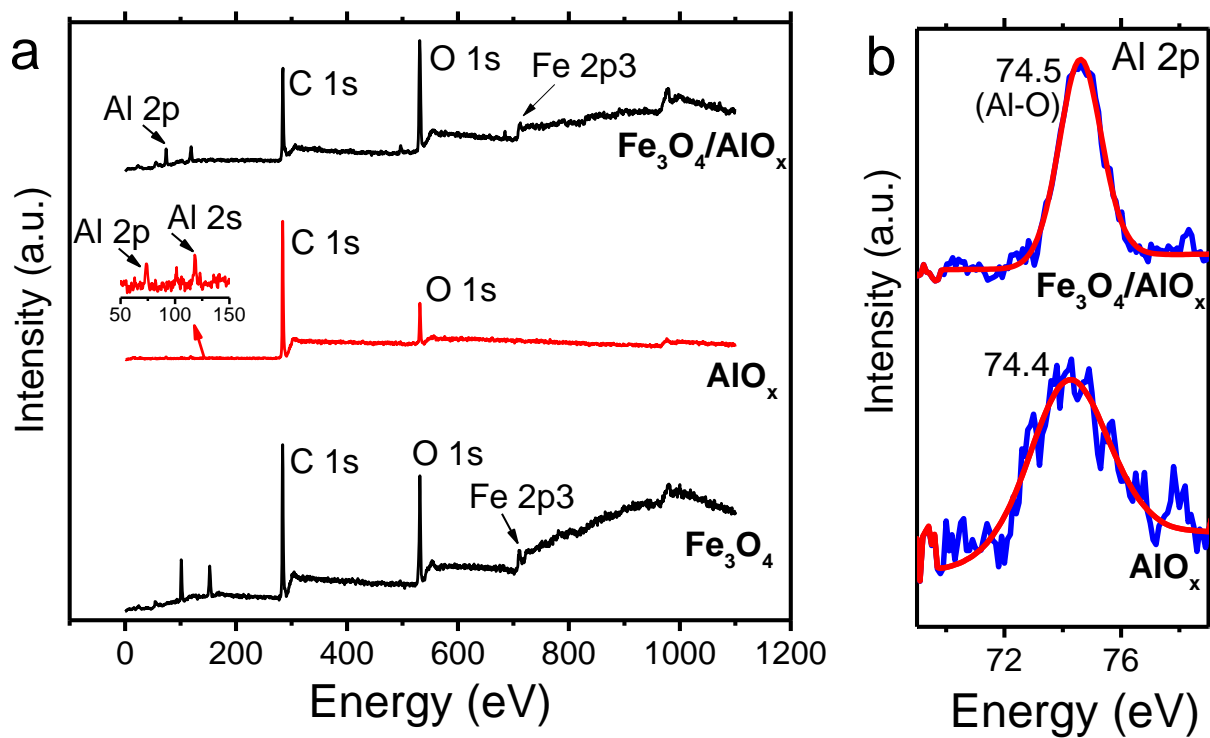


Figure S7. (a) Survey XPS spectra of AlO_x , Fe_3O_4 and $\text{Fe}_3\text{O}_4/\text{AlO}_x$ (50% Al content). Inset shows magnified Al 2p and Al 2s region (50 to 150 eV); (b) High resolution XPS spectra of Al 2p of AlO_x and $\text{Fe}_3\text{O}_4/\text{AlO}_x$ (50% Al content).

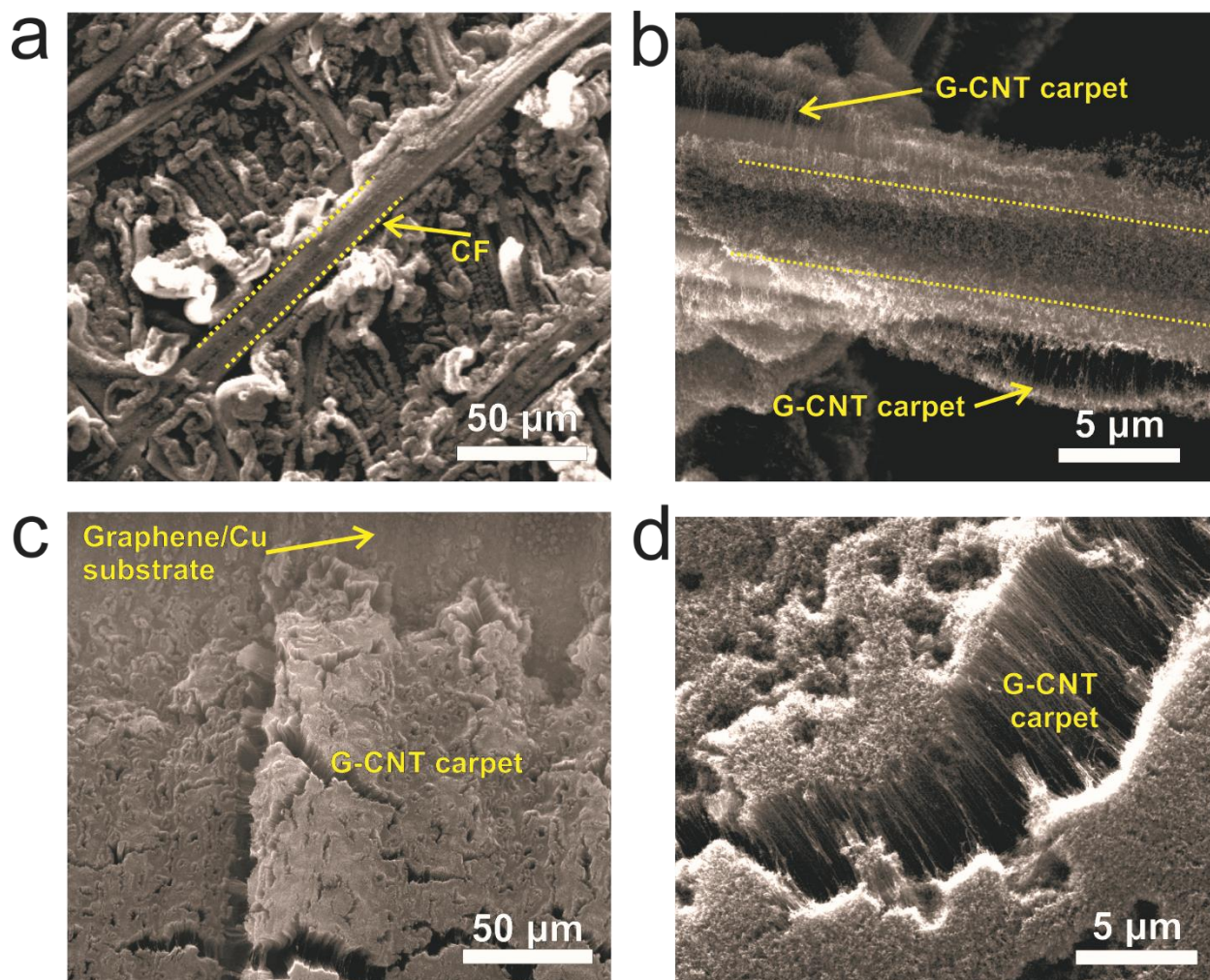


Figure S8. SEM images of the GCNT anode and cathode used in the composition of the LIC. (a, b) SEM images of the GCNT (used as cathode) on CF at low and high magnification. GCNT carpets portions are highlighted over the fiber structure; (c, d) SEM images of the GCNT grown G-Cu substrate (used as anode). Substrate and GCNT carpet are highlighted in the images.

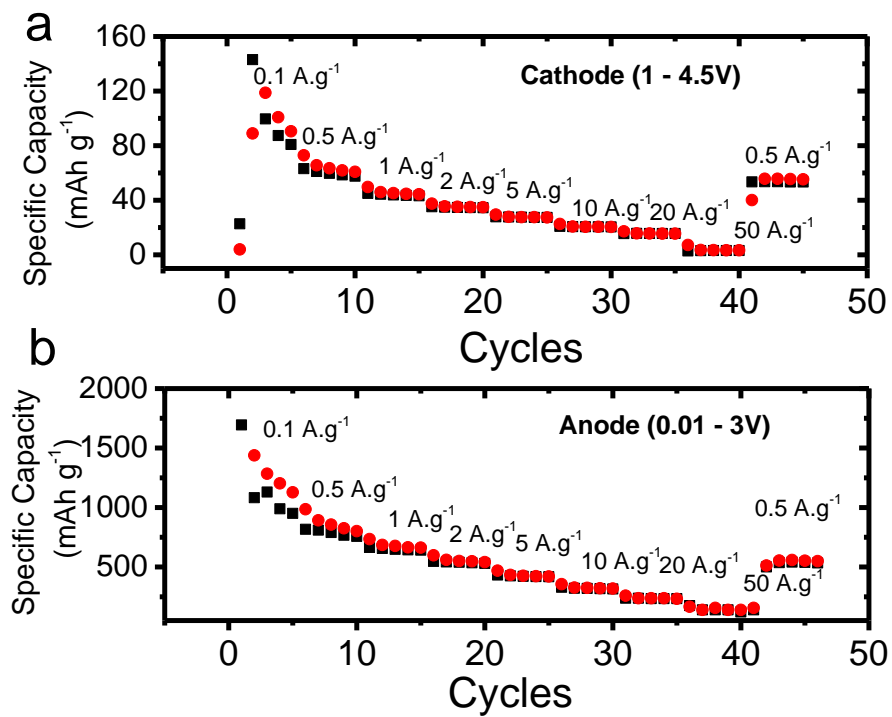


Figure S9. Rate testing of half-cells of GCNT as (a) cathode and (b) anode.

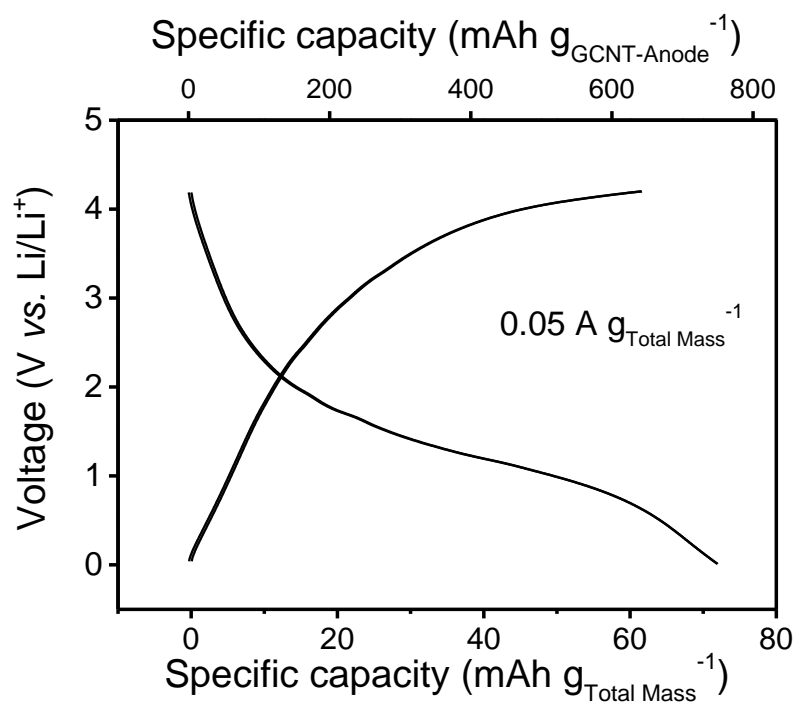


Figure S10. Charge/discharge curves of the GCNT LIC (0.05 A g⁻¹).

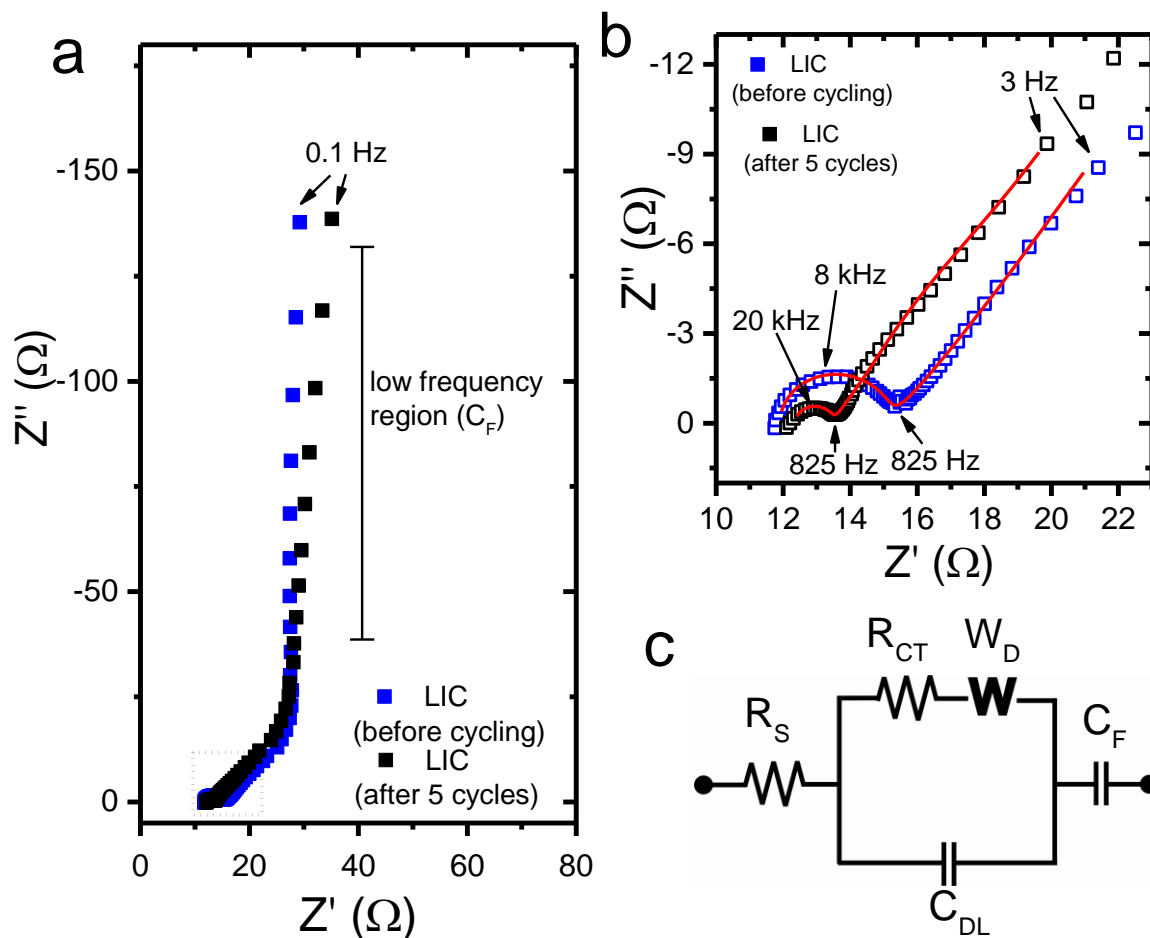


Figure S11. Impedance spectra of GCNT LIC. (a) Nyquist plot at open circuit potential (OCP) of GCNT LIC before cycling and after 5 complete cycles. The LIC were at the discharged state during the impedance measurement. The dotted square indicates the high frequency region. (b) High and mid-frequency Nyquist plot. The red curve indicates the fitting of the equivalent circuit over the experimental data. (c) Equivalent circuit used to fit the experimental data. Labels: R_S – series resistance, R_{CT} – charge transfer resistance, W_D – Warburg diffusion resistance, C_{DL} – double layer capacitance, C_F – faradaic capacitance (or polarizable capacitance).

Discussion of EIS data (Figure S11).

The impedance spectra of GCNT LIC is shown in Figure S11. The impedance was measured before the LIC testing and after the 5 complete cycles in the range of 10 mHz to 1 MHz, in which the devices were at the discharged state under equilibrium open circuit potential (OCP) (Figure S11a). The high to mid-frequency region is associated with the series resistance (combined resistance of the current collector and electrolyte), charge transfer resistance and Warburg diffusion resistance (Figure S11b). The low frequency impedance shows a straight vertical line. In the low frequency region, the ideal capacitance behavior would generate a perfectly parallel line to the Z'' axis.¹ This profile was already observed in other types of devices and CNT-based capacitors^{2,3} and indicates an almost ideal capacitive behavior whose mechanism is based on mass transfer to the electrode, hence the term mass or faradaic capacitance. The equivalent circuit used to modeling the experimental data is represented in Figure S11c. The fitted curves are displayed as the red curves in the Figure S11b. The calculated parameters (R_s – series resistance, R_{CT} – charge transfer resistance, W_D – Warburg diffusion resistance, C_{DL} – double layer capacitance, C_F – faradaic capacitance) are shown in Table S1. The values of impedances and capacitances for this system are consistent and comparable with other reports.^{1,4}

Table S1. Fitting parameters of impedance spectra of GCNT LIC.

	R_s	R_{CT}	C_{DL}	A_w^*	C_F
Initial stage	11.8 Ω	3.1 Ω	9.7 μF	18.6 $\Omega s^{-0.5}$	23.1 mF
After 5 cycles	12.34 Ω	1.1 Ω	4.9 μF	21.7 $\Omega s^{-0.5}$	13.4 mF

* Warburg coefficient $A_w (\Omega s^{-0.5})$

The initial cycling of the LIC starts by a discharge process, in which the fresh GCNT cathode is lithiated. The Li ion source is the previously lithiated GCNT anode. In this process a SEI layer must be formed over the cathode. The series resistance (R_s) does not change significantly (11.8 to 12.34 Ω) indicating the stability of the seamless connection of basal carbon plane and the CNT carpet. The double layer (C_{DL}) and faradaic (C_F) capacitances, which are dependents on the active surface area, change after the first 5 cycles as the result of the SEI formation. The decrease in R_{CT} can be related to a more open structure of the GCNT, induced by the initial cycling of the LIC. The value of the Warburg coefficient does not change significantly and indicates that diffusion in the bulk of the GCNT electrode is maintained after the SEI formation. This value of Warburg coefficient is significantly lower than similar CNT supercapacitors.¹ A lower value indicates a good rate capability, as we tested in the Figure 5 of the manuscript. The good rate capability is also corroborated by the frequency transition of ~ 825 Hz from the high frequency semi-circle to the mid-frequency line (Figure S11b). This so called “kink” frequency (f_K) indicates the frequency at which the diffusion of Li ions occurs into the bulk of the electrode. In Fig, S11b, the Z' value associated with this frequency is lower after the 5 cycles ($\sim 13 \Omega$) compared to the initial resistance ($\sim 16 \Omega$). The high value of this frequency (~ 825 Hz), compared to other carbonaceous materials (pure SWCNT ~ 221 Hz, activated carbon ~ 40 Hz),^{1,5} indicates that the diffusion can take place faster in our GCNT electrode and, therefore, it is consistent with our rate results.

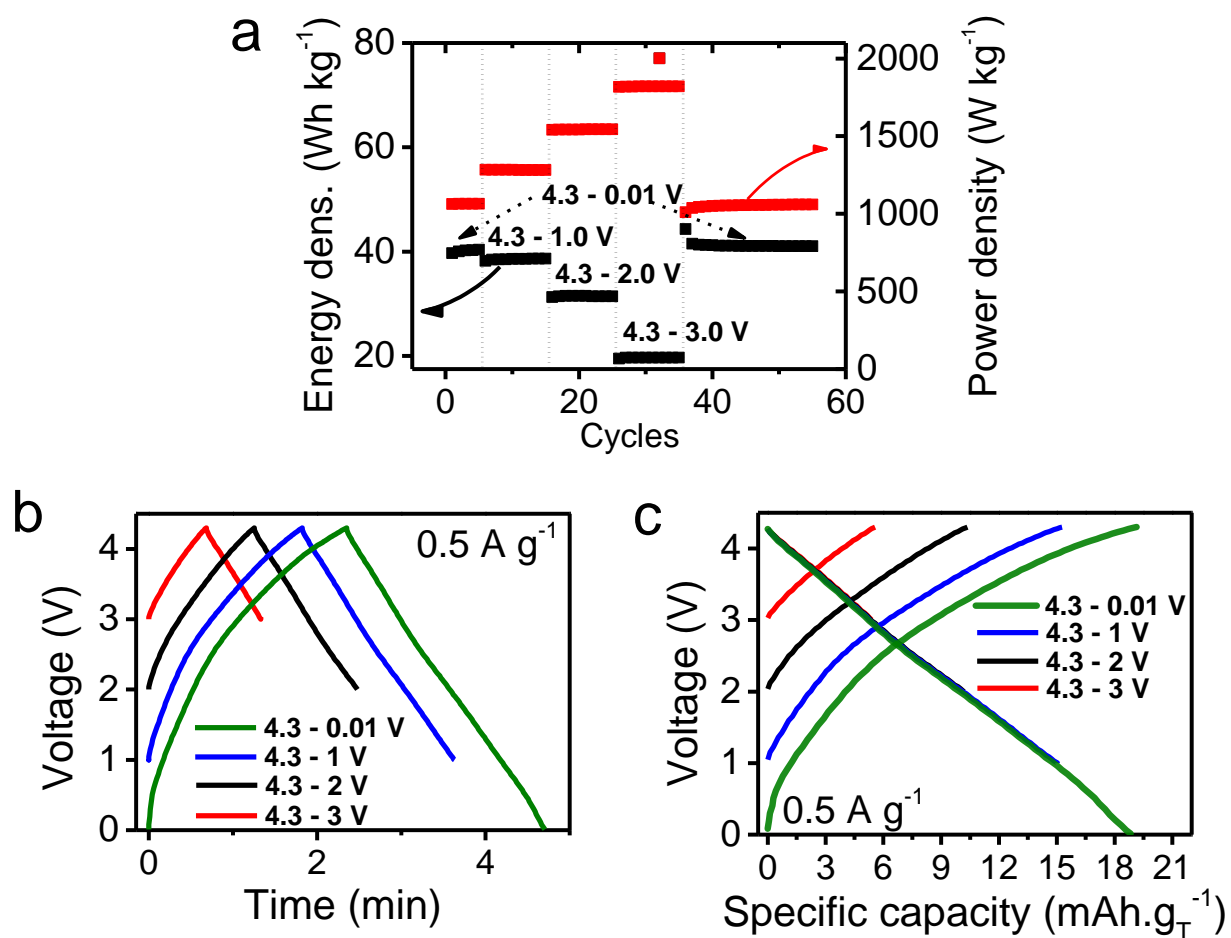


Figure S12. (a) Cycling stability of energy density and power density of the LIC tested at different voltage ranges starting at 4.3 to 0.01 V, 4.3 to 2 V, 4.3 to 1 V and back to 4.3 to 0.01 V (b-c) Charge/discharge curves of LIC at different voltage ranges expressed in voltage vs time and voltage vs specific capacity, respectively. The charge/discharge were run at 0.5 A g^{-1} .

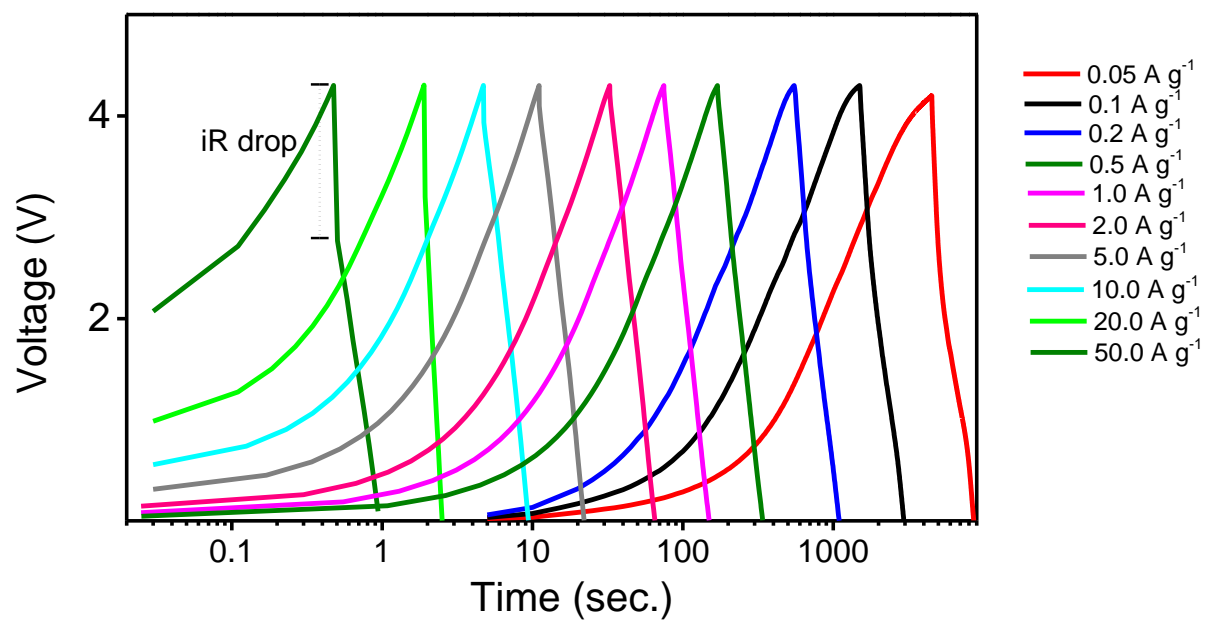


Figure S13. Charge/discharge curves of GCNT LIC at different rates. iR drop (voltage drop) contribution is demonstrate at the highest rate curve (50 A g⁻¹).

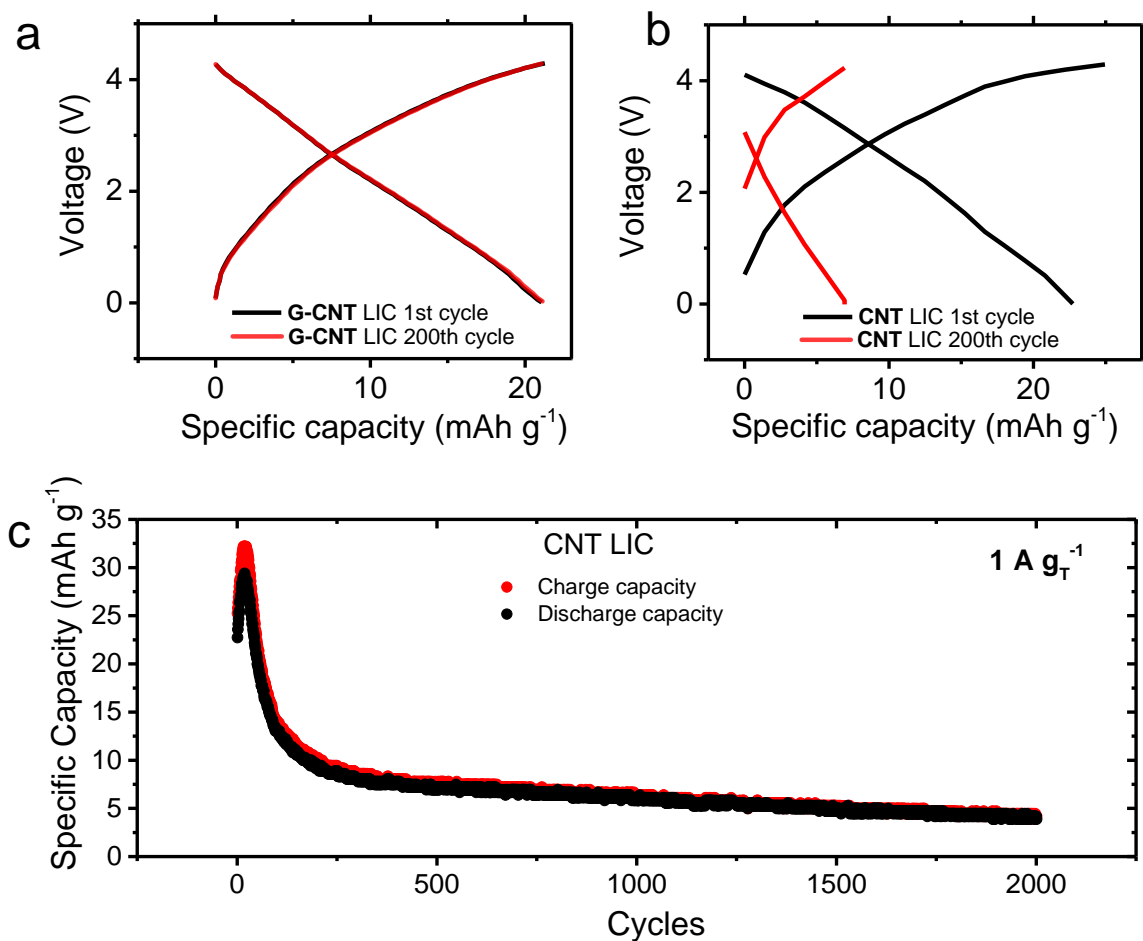


Figure S14. (a) Charge/discharge curve of the GCNT LIC in the long-range testing stability. The GCNT LIC displays the same capacity after 200 cycles. (b) Charge/discharge curves of the control LIC, produced using SWCNTs as the active materials for the LIC. The 200th cycle show less capacity compared to the first cycle test, indicating decomposition of the electrode. The full range stability is shown in Figure 5e of the manuscript. (c) Long-range stability of the CNT LIC showing capacity fading over 2000 cycles.

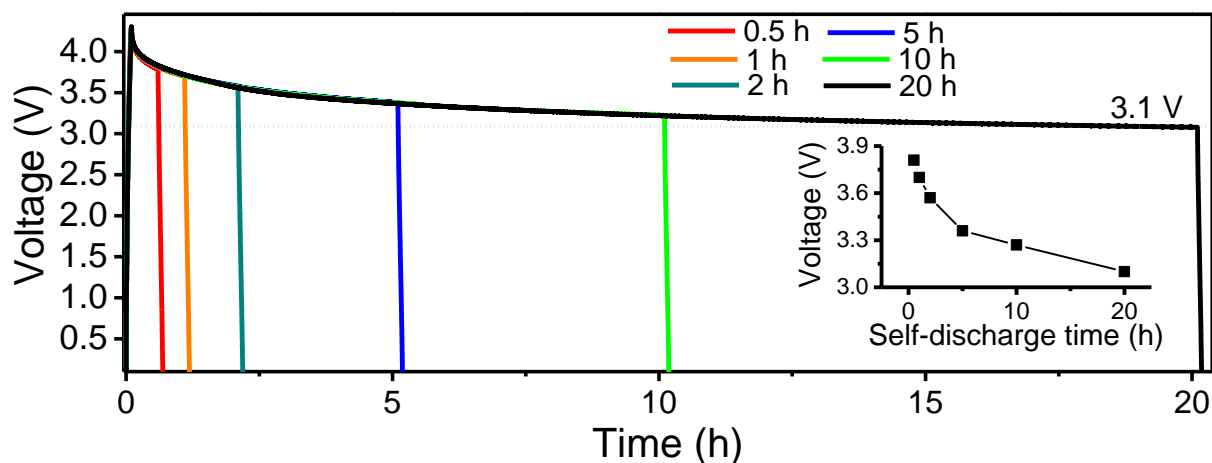


Figure S15. Voltage vs time graph showing the self-discharge of the GCNT LIC at different resting times (from 0.5 to 20 h). Charge and discharge rate were set to $1 \text{ A g}_\text{T}^{-1}$ Inset: voltage drop per self-discharge time.

References

1. Masarapu, C.; Zeng, H. F.; Hung, K. H.; Wei, B. Effect of Temperature on the Capacitance of Carbon Nanotube Supercapacitors. *ACS Nano* **2009**, *3*, 2199-2206.
2. Gu, T.; Wei, B. Fast and Stable Redox Reactions of MnO_2/CNT Hybrid Electrodes for Dynamically Stretchable Pseudocapacitors. *Nanoscale* **2015**, *7*, 11626-11632.
3. Chen, T.; Peng, H.; Durstock, M.; Dai, L. High-performance Transparent and Stretchable All-Solid Supercapacitors based on Highly Aligned Carbon Nanotube Sheets. *Sci. Rep.* **2013**, *4*, 3612
4. Wang, C.; Appleby, A. J.; Little, F. E. Electrochemical Impedance Study of Initial Lithium Ion Intercalation Into Graphite Powders. *Electrochim. Acta* **2001**, *46*, 1793-1813.

5. Farma, R.; Deraman, M.; Awitdrus; Talib, I.A.; Omar, R.; Manjunatha, J.G.; Ishak, M.M.; Basri, N.H.; Dolah, B. N. M. Physical and Electrochemical Properties of Supercapacitor Electrodes Derived from Carbon Nanotube and Biomass Carbon. *Int. J. Electrochem. Sci.* **2013**, 8, 257-273.